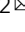## ARTICLE

Check for updates

Phonon-dressed states in an organic Mott insulator

Naoki Sono[1,3], Takashi Otaki [1,3], Takayuki Kitao[1], Takashi Yamakawa [1], Daiki Sakai[1], Takeshi Morimoto[1], Tatsuya Miyamoto [1✉] & Hiroshi Okamoto[1,2✉]

In an electronic system of solids excited by a femtosecond laser pulse, new quantum states called photon-dressed states are created via the coupling of original electron wavefunctions and periodic electric fields of light. The study of photon-dressed states is a central issue in nonlinear optical science, as a coherent response associated with a photon-dressed state can cause ultrafast optical-switching phenomena. In general, however, phase-sensitive dynamics of photon-dressed states are difficult to observe due to their short lifetime. Here, we show that excitation of the organic Mott insulator potassium-tetracyanoquinodimethane with a strong mid-infrared pulse induces a couple of intramolecular vibrations, which add temporally periodic potentials to the electronic system, giving rise to phonon-dressed states in the picosecond time domain. Through sub-cycle spectroscopy using a phase-stable mid-infrared pulse as an excitation and an ultrashort visible pulse as a probe, we observe optical radiation consisting of four kinds of coherent oscillations with double, sum, and differential frequencies of two intramolecular vibrations. The probe-energy dependence of each oscillation can be well interpreted with phonon-dressed states in the framework of Floquet theory. These findings open a possibility for Floquet engineering in correlated electron materials with strong charge–phonon couplings.

[1] Department of Advanced Materials Science, University of Tokyo, Kashiwa, Chiba 277-8561, Japan. [2] National Institute of Advanced Industrial Science and Technology (AIST)-University of Tokyo Advanced Operando-Measurement Technology Open Innovation Laboratory (OPERANDO-OIL), AIST, 5-1-5 Kashiwanoha, Kashiwa, Chiba 277-8561, Japan. [3]These authors contributed equally: Naoki Sono, Takashi Otaki. ✉email: miyamoto@k.u-tokyo.ac.jp; okamotoh@k.u-tokyo.ac.jp

Floquet theory suggests that the application of a periodic perturbation with frequency Ω to an electronic system creates new states at the energy positions separated from an original electronic level by integral multiples of $\hbar\Omega$[1–3]. These states are called "dressed states". A prototypical example is a photon-dressed state[4–10], which is created by the interaction of an electronic state with an oscillatory electric field of light. In the case that a coherent light–electron interaction occurs, ultrafast optical switching and wavelength conversion associated with photon-dressed states can be achieved based on optical Stark effects[4,7,11–14] and sideband emissions[5,8,10,15–21], respectively. Using a terahertz or mid-infrared pump pulse, sub-cycle detection of photon-dressed states is possible[8,19], although it is generally difficult because the photon-dressed states disappear within the duration of the pump pulse.

Several theoretical studies indicate that a dressed state can also be created by applying a periodic potential of phonons to an electronic system via electron–phonon coupling[3,22,23]. Such a dressed state, referred to as a "phonon-dressed state", can exist during the lifetime of the phonon, providing an opportunity to investigate the formation and annihilation dynamics of optically allowed dressed states by detecting optical radiation from each dressed state in the time domain. An effective way to produce a phonon-dressed state is to resonantly excite an infrared-active phonon with an intense laser pulse. In Fig. 1a, we exemplify optical radiations from phonon-dressed states. Here, $|\varphi_a\rangle$ ($|\varphi_f\rangle$) is an original one-photon-allowed (forbidden) state. $|\varphi_a, n\rangle$ and $|\varphi_f, n\rangle$ show the n-phonon-dressed states of $|\varphi_a\rangle$ and $|\varphi_f\rangle$, respectively. When the excited phonon is infrared-active, $|\varphi_a, \text{even number}\rangle$ and $|\varphi_f, \text{odd number}\rangle$ are one-photon-allowed states, and thus radiative transitions from those states can occur as shown by the colored arrows in Fig. 1a.

Here, we report the sub-cycle observation of phonon-dressed states using a pump-probe technique. There are two favorable conditions for creating phonon-dressed states: a phonon mode with a large oscillator strength and a strong electron–phonon coupling, which cause effective mixing of electron wavefunctions in the original excited states. Considering these conditions, we choose the organic molecular compound potassium-tetracyanoquinodimethane (K-TCNQ)[24]. In this compound, totally symmetric (a_g) modes of

intramolecular vibrations of each molecule are strongly coupled to intermolecular charge transfer, which results in infrared-activated with large oscillator strength. By resonantly exciting these phonons with a femtosecond laser pulse, we observe sideband emission ascribed to the formation of phonon-dressed states associated with the intramolecular transition using the sub-cycle spectroscopy (Fig. 1b). This achievement of the ultrafast creation and detection of phonon-dressed states opens a possibility for Floquet engineering with phonon degrees of freedom.

Results

Steady-state polarized reflectivity spectra. In K-TCNQ, an electron is transferred from K to TCNQ, and TCNQ$^-$ anions are one-dimensionally stacked along the a-axis as shown in Fig. 1c. The π-electron band consisting of a singly occupied molecular orbital (SOMO) is half-filled (Fig. 1d). Because of the large on-site Coulomb repulsion energy U on each TCNQ$^-$ overcoming the electron transfer integral t between two neighboring molecules, this compound behaves as a Mott insulator[25]. Spins ($S = 1/2$) of electrons localized on each molecule form a one-dimensional (1D) antiferromagnetic spin system. Due to the spin-Peierls mechanism, 1D molecular stacks are dimerized even at room temperature[24,25] (Fig. 1c).

To excite the phonons, we focus on the a_g modes of intramolecular vibrations of TCNQ, which are infrared-inactive in an isolated molecule, but activated in a TCNQ$^-$ dimer. This is because each a_g mode modulates the energy of the SOMO of TCNQ$^-$ via electron-intramolecular-vibration (EMV) coupling, and an out-of-phase combination of a_g modes of two molecules gives rise to an intermolecular charge transfer within the dimer, generating a large dipole moment along the a-axis[26] as illustrated in Fig. 1d.

In Fig. 2a, we show the steady-state reflectivity (R) spectra with electric fields E of light parallel ($//$) and perpendicular ($\perp$) to the a-axis. The broad structure around 1 eV for $E//a$ is a charge-transfer transition, (TCNQ$^-$, TCNQ$^-$) → (TCNQ^0, TCNQ^{2-})[27]. The structure around 2 eV for $E\perp a$ is the intramolecular transition from highest occupied molecular orbital (HOMO) to SOMO in TCNQ$^-$ (see the inset)[27,28], which creates a Frenkel
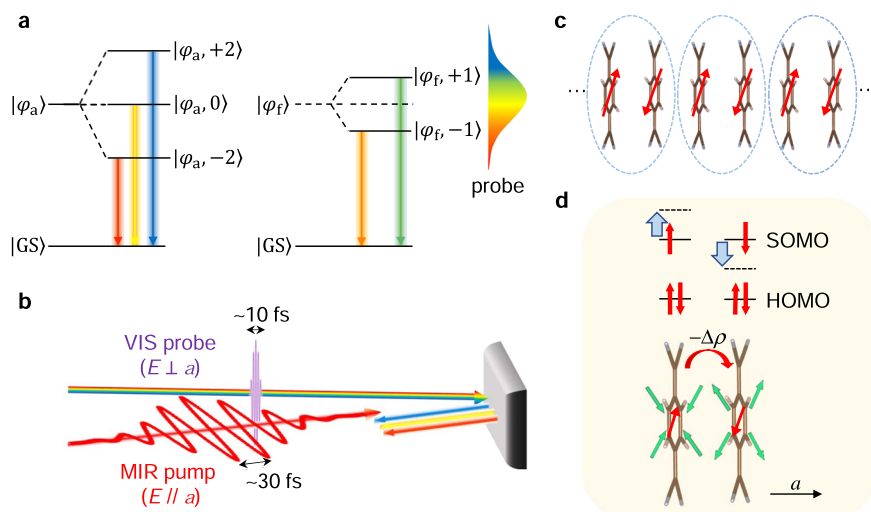

Fig. 1 Observation of phonon-dressed states in a dimerized organic Mott insulator of K-TCNQ. a Schematic energy levels of phonon-dressed states. $|\varphi_a\rangle$ ($|\varphi_f\rangle$) is an originally one-photon-allowed (forbidden) excited state and $|GS\rangle$ is a ground state. $|\varphi_{a,f}, n\rangle$ is an n-phonon-dressed state. Colored arrows show light emissions from phonon-dressed states. **b** Schematic of the mid-infrared (MIR)-pump visible (VIS)-reflectivity-probe measurement. **c** A 1D dimerized TCNQ$^-$ stack in K-TCNQ. **d** Schematic of an out-of-phase intramolecular vibration (a_g mode) in a dimer, which is infrared-activated via the electron-intramolecular-vibration (EMV) coupling. This out-of-phase vibration modulates singly occupied molecular orbital (SOMO) levels and induces a partial charge transfer ($-\triangle\rho < 0$) between two molecules in a dimer. HOMO represents the highest occupied molecular orbital.
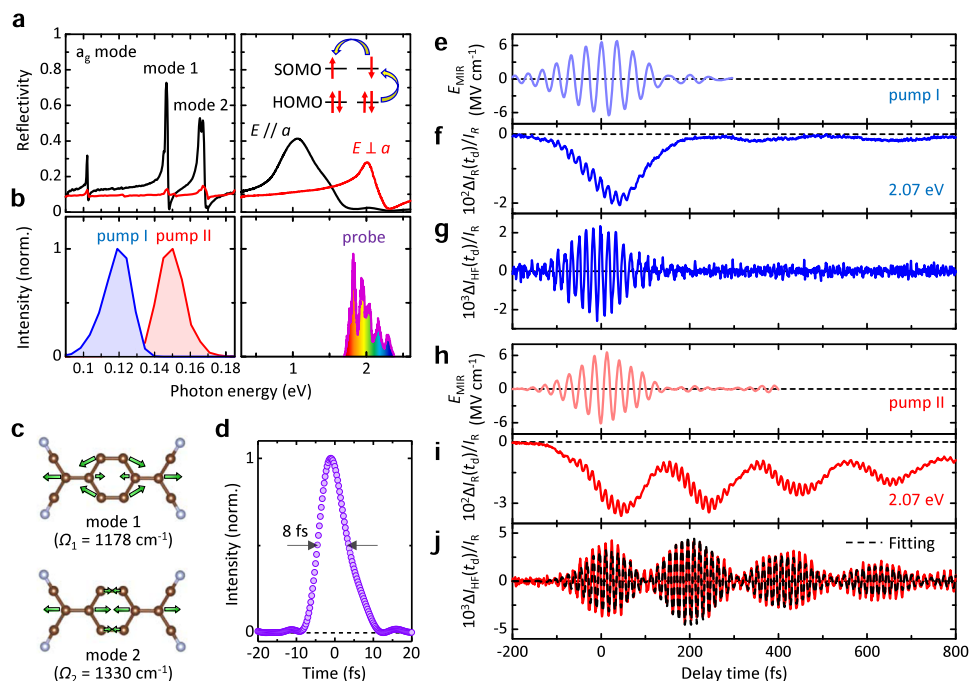
Fig. 2 Optical responses associated with phonon-dressed states generated by a mid-infrared pulse in K-TCNQ. a Polarized reflectivity spectra of K-TCNQ. SOMO and HOMO represent a singly occupied molecular orbital and a highest occupied molecular orbital, respectively. **b** The spectra of mid-infrared pulses for pump I and pump II, and of a visible-probe pulse. **c** Schematics of atomic motions in $a_g \nu_5$ mode with $\Omega_1 = 1178$ cm^{-1} and $a_g \nu_4$ mode with $\Omega_2 = 1330$ cm^{-1}. **d** The intensity envelope of the visible-probe pulse. **e–j** The electric-field waveform of the mid-infrared pump pulse (**e, h**), the time characteristic of the optical response, $\Delta I_R(t_d)/I_R$, at 2.07 eV (**f, i**), and the time characteristic of the high-frequency oscillatory component (**g, j**) for (**e, f**) off-resonant excitation (pump I) and (**h–j**) resonant excitation of a_g mode vibrations (pump II). The black broken line shown in **j** indicates the fitting curve.

exciton. Two sharp structures observed at the frequencies of $\Omega_1 = 1178$ cm^{-1} and $\Omega_2 = 1330$ cm^{-1} in the mid-infrared region are ascribed to the above-mentioned a_g modes of TCNQ$^-$ (modes 1 and 2, respectively) activated via EMV coupling[29,30]. The atomic motions of each mode obtained from ab initio calculations are illustrated in Fig. 2c (see Supplementary Note 1).

Mid-infrared pump pulse and visible-probe pulse. Figure 2b shows the spectra of the phase-stable mid-infrared pump pulses in two conditions, pump I and pump II; pump II, with a central frequency of 1211 cm^{-1}, resonantly excites two a_g modes, whereas pump I, with a central frequency of 970 cm^{-1}, does not. The electric-field waveforms of mid-infrared pulses for pump I and pump II are shown in Fig. 2e, h, respectively.

To detect phonon-dressed states, we use an ultrashort visible-probe pulse polarized perpendicular to the a-axis. Its spectrum, drawn in iridescent in Fig. 2b, covers the intramolecular transition of TCNQ$^-$. We aim to detect optical radiation from its phonon-dressed states in the reflection configuration as illustrated in Fig. 1b. Figure 2d shows a temporal profile of the probe pulse intensity. Its width is approximately 8 fs, much shorter than the periods of a_g modes 1 (28 fs) and 2 (25 fs). This condition facilitates sub-cycle detection of optical radiation.

Sub-cycle detection of oscillatory signals in optical radiation from phonon-dressed states. In Fig. 2f, i, we show the time profiles of optical radiation, $\Delta I_R(t_d)/I_R$, at 2.07 eV by the mid-infrared pump pulses for the conditions of pumps I and II, which were measured with the pump-probe experiments illustrated in Fig. 1b. t_d is the delay time of the probe pulse relative to the pump pulse. The electric-field amplitude of the mid-infrared pump pulses (Fig. 2e, h) is 6 MV cm^{-1} in common. Here, I_R is the

intensity of the reflected probe pulse without a pump pulse, and $\Delta I_R(t_d)$ is its intensity change with a pump pulse, which includes radiation from dressed states. In the off-resonant phonon excitation with pump I (Fig. 2e), $\Delta I_R(t_d)/I_R$ consists of a background component coincident with the envelope of the square of mid-infrared electric fields and a high-frequency oscillatory component. The latter is shown in Fig. 2g. Its frequency (2001 cm^{-1}) is almost equal to double the central frequency of the pump pulse (970 cm^{-1}). No delayed responses were observed. These ultrafast responses are ascribed to photon-dressed states.

In the resonant phonon excitation with pump II (Fig. 2h), $\Delta I_R(t_d)/I_R$ includes at least three types of long-lived components that survive after the pump pulse diminishes: the decrease in the reflected probe pulse with a long decay time, the low-frequency oscillatory component, $\Delta I_{LF}(t_d)/I_R$, with a period of ~200 fs, and the high-frequency oscillatory component, $\Delta I_{HF}(t_d)/I_R$, with a period of ~14 fs. The extracted time profile of $\Delta I_{HF}(t_d)/I_R$ is shown in Fig. 2j, in which a prominent waviness is seen. This indicates that $\Delta I_{HF}(t_d)/I_R$ consists at least of two oscillations with similar frequencies.

To clarify the origin of the high- and low-frequency oscillatory components, we perform Fourier transformations of $\Delta I_R(t_d)/I_R$. The obtained power spectra are shown by red circles in Fig. 3a, b. Figure 3d exhibits steady-state absorption (ε_2) for a_g modes 1 and 2, while its horizontal scale is half that in Fig. 3b, c. The power spectrum in the mid-infrared region shows three oscillations labeled as A, B, and C, the frequencies of which are $\Omega_A = 2370$ cm^{-1}, $\Omega_B = 2527$ cm^{-1}, and $\Omega_C = 2685$ cm^{-1}, respectively. Ω_A, Ω_B, and Ω_C correspond to the sum of the frequencies of modes 1 and 2, which are $2\Omega_1 = 2356$ cm^{-1}, $\Omega_1 + \Omega_2 = 2508$ cm^{-1}, and $2\Omega_2 = 2660$ cm^{-1}, respectively. The power spectrum in the far-infrared region shows an oscillation labeled as D. Its frequency $\Omega_D = 158$ cm^{-1} is almost equal to the
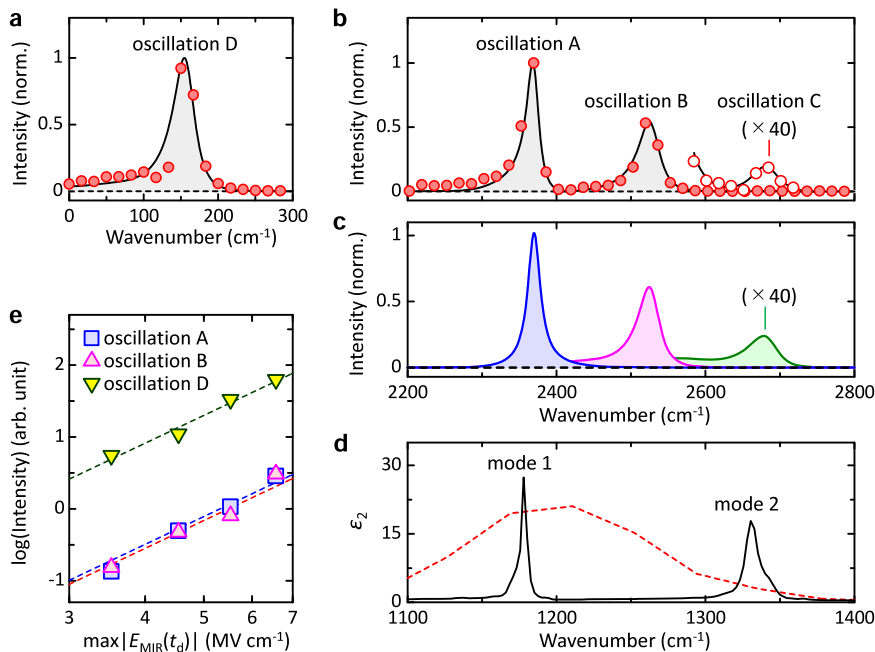
Fig. 3 High- and low-frequency oscillatory components in optical responses associated with phonon-dressed states in K-TCNQ. a The Fourier power spectrum of the low-frequency oscillation D in $\Delta I_R(t_d)/I_R$ (red circles) and the calculated oscillation obtained from the fitting analysis of the time characteristic of $\Delta I_{LF}(t_d)/I_R$ (the black line). **b** The Fourier power spectrum of the high-frequency oscillatory component $\Delta I_{HF}(t_d)/I_R$ (red circles) and the fitting curve (the black line). **c** Spectra of three oscillations A–C obtained by the fitting analysis of the time characteristic of the high-frequency oscillatory component $\Delta I_{HF}(t_d)/I_R$ in $\Delta I_R(t_d)/I_R$ shown in Fig. 2j. **d** The ϵ_2 spectrum along the a-axis. The spectrum of the mid-infrared pump pulse (pump II) is shown by the red broken line. **e** Intensities of three oscillatory components A, B, and D, obtained from the fitting analyses of $\Delta I_{HF}(t_d)/I_R$ and $\Delta I_{LF}(t_d)/I_R$. The error bars, defined as one standard deviation of the least-squared fit, are smaller than the data points.

subtraction between the frequencies of modes 1 and 2, $\Omega_2 - \Omega_1 = 152$ cm^{-1}. These results indicate that the high- and low-frequency oscillations are caused by the second-order terms of the a_g-mode vibrations. The first-order terms become zero because K-TCNQ is invariant for the a-axis inversion.

Figure 3e shows how the integrated intensities of the power spectra, I_A, I_B, and I_D, for oscillations A, B, and D, respectively, depend on the maximum electric-field amplitude of the mid-infrared pulse, $\max|E_{MIR}(t_d)|$. All the intensities are proportional to $(\max|E_{MIR}(t_d)|)^4$. This means that amplitudes of each oscillation are proportional to $(\max|E_{MIR}(t_d)|)^2$. These results are explained in the following way. The oscillatory signals of the reflectivity changes, $\Delta I_{LF}(t_d)/I_R$ and $\Delta I_{HF}(t_d)/I_R$, are due to the electronic state modulations by the out-of-phase combinations of each a_g mode in each dimer. Therefore, they are expected to be proportional to $[g_{S1}Q_1(t_d) + g_{S2}Q_2(t_d)]^2$. Here, $Q_1(t_d)$ and $Q_2(t_d)$ are the normal coordinates of mode 1 with frequency Ω_1 and mode 2 with frequency Ω_2, respectively. g_{S1} and g_{S2} are the EMV coupling constant of mode 1 and mode 2 defined by $g_{S1} = \sqrt{\frac{\hbar}{2\Omega_1}}\frac{\partial \epsilon_S}{\partial Q_1}$ and $g_{S2} = \sqrt{\frac{\hbar}{2\Omega_2}}\frac{\partial \epsilon_S}{\partial Q_2}$, respectively, which determine how large the energy ϵ_S of SOMO changes with the coordinate $Q_i(t_d)$ $(i=1, 2)$. Thus, the oscillatory signals include the components proportional to $[Q_1(t_d)]^2$, $[Q_2(t_d)]^2$, and $Q_1(t_d)Q_2(t_d)$. As a result, the high-frequency signals, $\Delta I_{HF}(t_d)/I_R$, consists of oscillatory components with the frequencies of $2\Omega_1$, $2\Omega_2$, and $\Omega_1 + \Omega_2$, and the low-frequency signal, $\Delta I_{LF}(t_d)/I_R$, is the oscillation with the frequency of $\Omega_2 - \Omega_1$. Since $Q_i(t_d)$ $(i=1, 2)$ is proportional to the electric-field amplitude, $\max|E_{MIR}(t_d)|$, the amplitude of each oscillatory signal is proportional to the square of $\max|E_{MIR}(t_d)|$, and the

integrated intensities I_A, I_B, and I_D are, therefore, proportional to $\max|E_{MIR}(t_d)|$ to the forth power as observed in Fig. 3e. Since all the oscillatory amplitudes in $\Delta I_R(t_d)/I_R$ are proportional to the square of $\max|E_{MIR}(t_d)|$, so that they can be also considered a kind of third-order nonlinear optical responses. Strictly speaking, the magnitudes of the oscillatory signals are affected by the effects of the EMV coupling associated with HOMO as well as SOMO, while the electric-field dependence does not change. This point is discussed in Supplementary Note 3.

The Fourier power spectrum of the oscillatory signals can also be deduced by the fitting analyses of the time evolutions of the oscillatory components using damped oscillators, which are reported in the Method section and Supplementary Note 2. The high-frequency oscillatory component is well reproduced by the fitting analyses as shown by the black solid line in Fig. 2j. The corresponding Fourier power spectrum is shown by the black solid line in Fig. 3a, b, which is in good agreement with that shown by the red circles in the same figures. The advantage of this fitting analysis is that we can deduce the spectrum of each oscillatory signal separately, which is also shown by the colored solid lines in Fig. 3c. This analysis is used to evaluate the probe-energy dependence of each oscillatory signal as discussed later.

Theoretical framework of optical radiation from phonon-dressed states based upon third-order optical nonlinearity. The optical radiation observed as the oscillatory signals in $\Delta I_R(t_d)/I_R$ is expected to originate from phonon-dressed states of the intramolecular transitions illustrated in Fig. 1a. To clarify the relation between the oscillatory signals and the phonon-dressed states, we formulated the oscillatory signals using the three-level model and the framework of the third-order optical nonlinearity, the details of which are reported in Supplementary Notes 3 and 4,
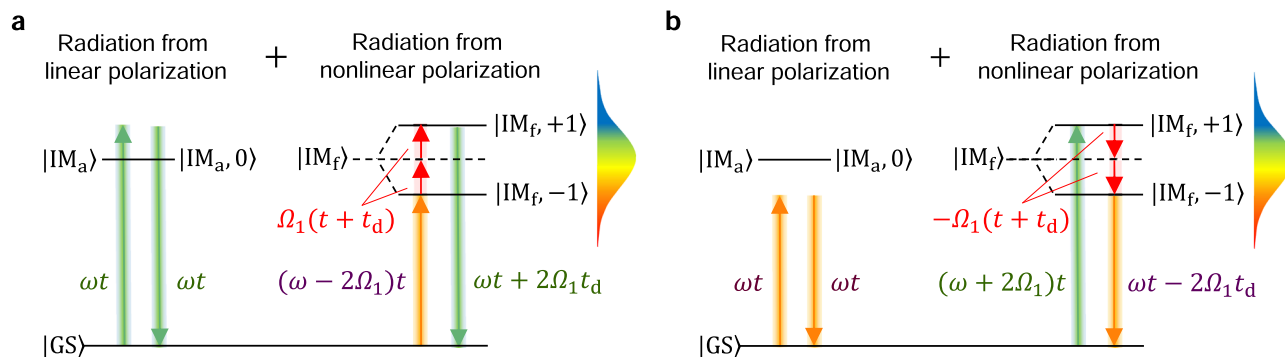
Fig. 4 Schematics of generation mechanism of high-frequency oscillations in reflectivity changes. a The case that only the mode 1 of the frequency of Ω_1 is excited by the mid-infrared pulse, and the state $|IM_f, +1\rangle$ is resonantly excited by the combination of three processes indicated by the arrows. The probe pulse covers the energies of the states $|IM_a\rangle$, $|IM_f, +1\rangle$, and $|IM_f, -1\rangle$. The linear absorption spectrum is broad and therefore the state $|IM_a\rangle$ is also excited. The radiation from the linear polarization of $|IM_a\rangle$ and that from the nonlinear polarization of $|IM_f, +1\rangle$ have the phase of ωt and $(\omega t + 2\Omega_1 t_d)$, respectively. t_d is the delay time of the probe pulse relative to the pump pulse. Those two radiations interfere with each other, giving rise to the oscillation of the frequency $2\Omega_1$ in the pump-probe signal. Phase part of each excitation and radiation is shown by colored characters. **b** The case that the state $|IM_f, +1\rangle$ is resonantly excited by the probe pulse. The radiation from the linear polarization of $|IM_a\rangle$ and that from the nonlinear polarization of $|IM_f, -1\rangle$ have the phase of of ωt and $(\omega t - 2\Omega_1 t_d)$ and interfere with each other, giving rise to the oscillation of the frequency $2\Omega_1$.

respectively. In this sub-section, we report the main part of the formulation.

In our formulation, we consider an isolated dimer and adopt a three-level model, which consists of the ground state $|GS\rangle$ and two excited states $|IM_a\rangle$ and $|IM_f\rangle$, which are the one-photon allowed and one-photon forbidden intramolecular excited states, respectively. The electronic states in a dimer are expressed using the following formula.

$$\left| \begin{array}{cc} LS & RS \\ LH & RH \end{array} \right\rangle \tag{1}$$

L and R show left and right site in a dimer, respectively. S and H represent the higher-energy and lower-energy orbital, which correspond to SOMO and HOMO in the original state, respectively (see Fig. 1d). An electron is expressed by an arrow, which shows the direction of each spin. For example, $\left| \begin{array}{cc} \uparrow & \downarrow \\ \uparrow\downarrow & \uparrow\downarrow \end{array} \right\rangle$ represents the lowest-energy state with an up-spin electron in LS and a down-spin electron in RS. By assuming that the intradimer transfer integrals are negligibly small compared to intramolecular Coulomb repulsion energy, the ground state is expressed as follows:

$$|GS\rangle = \frac{1}{\sqrt{2}}\left(\left| \begin{array}{cc} \uparrow & \downarrow \\ \uparrow\downarrow & \uparrow\downarrow \end{array} \right\rangle - \left| \begin{array}{cc} \downarrow & \uparrow \\ \uparrow\downarrow & \uparrow\downarrow \end{array} \right\rangle \right) \tag{2}$$

In the intramolecular excitations, we consider the excited states, $\left| \begin{array}{cc} \uparrow & \uparrow\downarrow \\ \uparrow\downarrow & \downarrow \end{array} \right\rangle$ and $\left| \begin{array}{cc} \uparrow\downarrow & \uparrow \\ \downarrow & \uparrow\downarrow \end{array} \right\rangle$, in which an up-spin electron is excited from HOMO to SOMO. The eigenstates can be expressed by the following two states, which should be nearly degenerate.

$$|IM_a\rangle = \frac{1}{\sqrt{2}}\left(\left| \begin{array}{cc} \uparrow & \uparrow\downarrow \\ \uparrow\downarrow & \downarrow \end{array} \right\rangle + \left| \begin{array}{cc} \uparrow\downarrow & \uparrow \\ \downarrow & \uparrow\downarrow \end{array} \right\rangle \right)$$
$$|IM_f\rangle = \frac{1}{\sqrt{2}}\left(\left| \begin{array}{cc} \uparrow & \uparrow\downarrow \\ \uparrow\downarrow & \downarrow \end{array} \right\rangle - \left| \begin{array}{cc} \uparrow\downarrow & \uparrow \\ \downarrow & \uparrow\downarrow \end{array} \right\rangle \right) \tag{3}$$

$|IM_a\rangle$ and $|IM_f\rangle$ are one-photon allowed and forbidden for $E \perp a$, respectively.

When the EMV coupling exists, radiations from the dressed states, $|IM_a, \pm 2n\rangle$ and $|IM_f, \pm(2n-1)\rangle$ (n: natural number), can occur. The energy of $|IM_a\rangle$ is approximately 2.0 eV, and $|IM_f\rangle$ is almost degenerate with $|IM_a\rangle$. Considering that the

energy of mode 1 (mode 2) is 0.146 eV (0.165 eV), the probe pulse ranging from 1.75 to 2.25 eV can cover only the dressed states $|IM_f, \pm 1\rangle$ associated with the originally one-photon forbidden excited state $|IM_f\rangle$, which will be responsible for the oscillatory signals in $\Delta I_R(t_d)/I_R$.

In this case, the radiation from the dressed states due to the nonlinear polarization with the frequency ω is considered to occur by the third-order nonlinear polarization $P^{(3)}$, which is proportional to $[g_{S1}Q_1 + g_{S2}Q_2]^2 E_{VIS}$. Here, E_{VIS} is the electric field of the probe pulse. Q_1 and Q_2 are generated by the forced oscillations of modes 1 and 2 by the mid-infrared pulse, respectively, so that the magnitude of $P^{(3)}$ is proportional to the product of E_{VIS} and the square of the mid-infrared electric field.

Hereafter, we consider only the high-frequency oscillatory signals to simplify the discussion. In the frequency domain, the third-order nonlinear polarization $P^{(3)}(\omega)$ with frequency ω originating from the higher dressed states $|IM_f, +1\rangle$ associated with mode 1 and mode 2 is dominated mainly by the terms of $\chi_{\Omega_1,\Omega_1}^{(3)}(\omega)Q_1(\Omega_1)Q_1(\Omega_1)E_{VIS}(\omega - 2\Omega_1)$, $\chi_{\Omega_2,\Omega_2}^{(3)}(\omega)Q_2(\Omega_2)Q_2(\Omega_2)$ $E_{VIS}(\omega - 2\Omega_2)$, and $\chi_{\Omega_1,\Omega_2}^{(3)}(\omega)Q_1(\Omega_1)Q_2(\Omega_2)E_{VIS}(\omega - \Omega_1 - \Omega_2)$. Here, $\chi_{\Omega_a,\Omega_b}^{(3)}(a, b = 1, 2)$ is third-order nonlinear susceptibility. $Q_1(\omega)$ and $Q_2(\omega)$ are the frequency dependences of the coordinates of mode 1 and 2, respectively, and $E_{VIS}(\omega)$ is the spectrum of the probe pulse. The linear polarization $P^{(1)}(\omega) = \varepsilon_0 \chi^{(1)} E_{VIS}(\omega)$ is also generated due to the transition from $|GS\rangle$ to the originally one-photon allowed state $|IM_a\rangle$. Compared to the radiation from $P^{(1)}(\omega)$, the radiations from $P^{(3)}(\omega)$ related to $\chi_{\Omega_1,\Omega_1}^{(3)}$, $\chi_{\Omega_2,\Omega_2}^{(3)}(\omega)$, and $\chi_{\Omega_1,\Omega_2}^{(3)}(\chi_{\Omega_2,\Omega_1}^{(3)})$ have the additional phase of $2\Omega_1 t_d$, $2\Omega_2 t_d$, and $(\Omega_1 + \Omega_2)t_d$, respectively. It is because the polarizations of frequency Ω_1 and Ω_2 due to the mode 1 and mode 2 vibrations are generated at a time t_d before the probe pulse is incident to the sample. In this situation, the two types of the radiations with the frequency ω from the polarizations of $P^{(1)}(\omega)$ and $P^{(3)}(\omega)$ interfere with each other, giving rise to the oscillations with the frequencies of $2\Omega_1$, $2\Omega_2$, and $(\Omega_1 + \Omega_2)$ in $\Delta I_R(t_d)/I_R$ as observed in the pump-probe signal. This mechanism of the oscillation generation with $2\Omega_1$ related to $\chi_{\Omega_1,\Omega_1}^{(3)}$ is illustrated in Fig. 4a, in which each arrow indicates the excitation by the probe pulse or the mid-infrared pulse. The phase part of

each optical process is written in the same figure. An oscillation of the frequency $2\Omega_1$ appears due to the interference between the radiation oscillating at ωt from $P^{(1)}(\omega)$ and the radiation oscillating at $\omega t + 2\Omega_1 t_d$ from $P^{(3)}(\omega)$. The oscillation related to the lower dressed state $|IM_f, -1\rangle$ occurs due to the similar mechanism as illustrated in Fig. 4b. As a result, the high-frequency oscillations with the frequencies of $2\Omega_1$, $2\Omega_2$, and $(\Omega_1 + \Omega_2)$ are expected to have two peaks separated by $2\Omega_1$, $2\Omega_2$, and $(\Omega_1 + \Omega_2)$, respectively, in the probe photon-energy dependence, that is, in the spectrum. As for the low-frequency oscillation with the frequency of $(\Omega_2 - \Omega_1)$, we can also consider the similar generation mechanism based upon the third-order optical nonlinearity.

Next, we show the relation between the radiation from the phonon-dressed states $|IM_f, \pm 1\rangle$ and the third-order nonlinear susceptibility $\chi^{(3)}_{\Omega_a, \Omega_b}$. The change in the intensity of the radiated light, $\Delta I_R(\omega, t_d)$, as a function of the delay time t_d is expressed as

$$\Delta I_R(\omega, t_d) = \left| \tilde{r}_y(\omega) E_{VIS}(\omega, t_d) + \Delta E_R(\omega, t_d) \right|^2 \\ - \left| \tilde{r}_y(\omega) E_{VIS}(\omega, t_d) \right|^2. \tag{4}$$

Here, $\tilde{r}_y(\omega)$ is the complex amplitude reflectivity and $\Delta E_R(\omega, t_d)$ is the change in the radiated electric field. The oscillatory component $\Delta I_{\Omega_a + \Omega_b}(\omega)$ of the oscillation frequency $\Omega_a + \Omega_b$ $(\Omega_a, \Omega_b = \Omega_1, \Omega_2)$ in $\Delta I_R(\omega, t_d)$ is expressed as follows:

$$\Delta I_{\Omega_a + \Omega_b}(\omega) \propto \xi_{\Omega_a, \Omega_b}(\omega)\chi^{(3)}_{\Omega_a, \Omega_b}(\omega)E_{VIS}(\omega - \Omega_a - \Omega_b)E^*_{VIS}(\omega) \\ + \left[\xi_{-\Omega_a, -\Omega_b}(\omega)\chi^{(3)}_{\Omega_{-a}, \Omega_{-b}}(\omega)E_{VIS}(\omega + \Omega_a + \Omega_b)E^*_{VIS}(\omega) \right]^* \tag{5}$$

Here, $\xi_{\pm\Omega_a, \pm\Omega_b}(\omega)$ is a parameter related to the linear optical constants. $\Delta I_{\Omega_a + \Omega_b}(\omega)$ depends not only on $E_{VIS}(\omega)$ but also on $E_{VIS}(\omega \pm (\Omega_a + \Omega_b))$. In Fig. 5a, we show the intensity spectrum

of the probe pulse $|E_{VIS}(\omega)|^2$ and the spectra shifted by $\pm 2\Omega_1$, $|E_{VIS}(\omega \pm 2\Omega_1)|^2$. $|E_{VIS}(\omega)|^2$ ranges from 1.75 to 2.25 eV. $2\hbar\Omega_1$ is approximately 0.3 eV, and thus $|E_{VIS}(\omega - 2\Omega_1)|^2$ and $|E_{VIS}(\omega + 2\Omega_1)|^2$ cover 2.05–2.55 and 1.45–1.95 eV, respectively. Therefore, for $\hbar\omega > 2$ eV ($\hbar\omega \le 2$ eV), the first (second) term in Eq. (5) dominates the high-frequency oscillations. Accounting for this experimental condition, we derive the spectrum of $\left|\chi^{(3)}_{\pm\Omega_a, \pm\Omega_b}(\omega)\right|^2$ as follows:

$$\left|\chi^{(3)}_{\pm\Omega_a, \pm\Omega_b}(\omega)\right|^2 \propto \frac{\left|\Delta I_{\Omega_a + \Omega_b}(\omega)\right|^2}{\left|\xi_{\pm\Omega_a, \pm\Omega_b}(\omega)E_{VIS}(\omega \mp \Omega_a \mp \Omega_b)E^*_{VIS}(\omega)\right|^2} \tag{6}$$
$$(+ \text{ for } \hbar\omega > 2 \text{ eV}, - \text{ for } \hbar\omega \le 2 \text{ eV})$$

The derivations of Eqs. (5) and (6) and the formula of $\xi_{\pm\Omega_a, \pm\Omega_b}(\omega)$ are detailed in Supplementary Note 4.

Probe photon-energy dependence of oscillatory signals in optical radiation from phonon-dressed states. By monochromizing the change of the radiation, $\Delta I_R(t_d)$, and obtaining the spectra of the high-frequency oscillations, we can verify the interpretation of the oscillatory signals mentioned in the previous sub-section. For this measurement, we also use a mid-infrared pulse exciting both a_g modes 1 and 2 as shown in Fig. 2a, although its electric-field waveform is slightly different from that shown in Fig. 2b (see Supplementary Note 5). Here, we focus only on the $\hbar\omega$-dependence of high-frequency oscillations A–C in $\Delta I_{HF}(t)$. Via the fitting procedure detailed in the Method section and Supplementary Note 2, we evaluate the time profile of each oscillatory component for various probe photon energies. From those data, we obtained each Fourier power spectrum and its integrated intensity I_A, I_B, and I_C as a function of $\hbar\omega$, which correspond to $|\Delta I_{\Omega_a + \Omega_b}(\omega)|^2$ in Eq. (6).
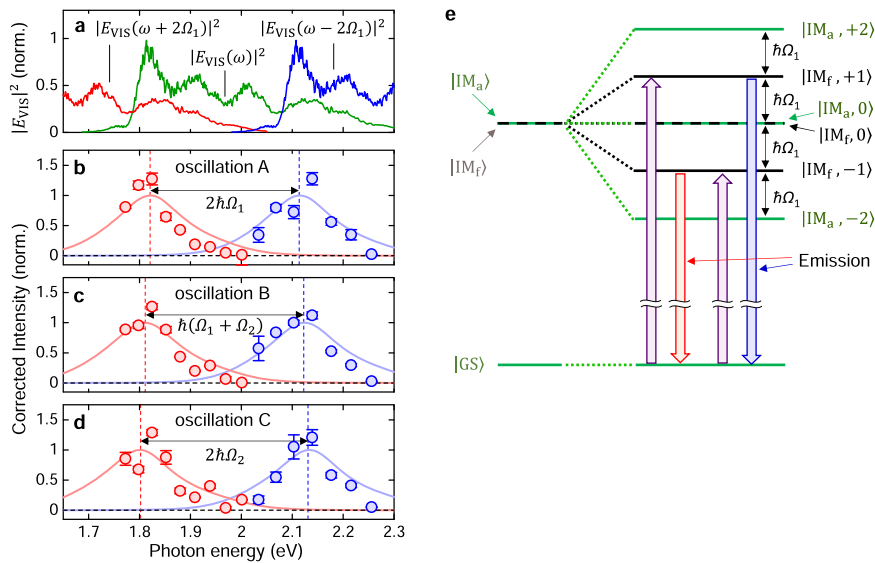

Fig. 5 Probe photon-energy dependence of high-frequency oscillations in optical responses associated with phonon-dressed states in K-TCNQ. a The power spectrum of the visible-probe pulse $|E_{VIS}(\omega)|^2$ and those shifted by $\pm 2\Omega_1$. **b–d** The corrected intensities of high-frequency oscillations A–C expressed by Eq. (6) for $\hbar\omega > 2$ eV (blue circles) and for $\hbar\omega \le 2$ eV (red circles). Blue and red lines show simulated spectra of $|\chi^{(3)}_{\pm\Omega_1, \pm\Omega_1}(\omega)|^2$ (**b**), $|\chi^{(3)}_{\pm\Omega_1, \pm\Omega_2}(\omega)|^2$ (**c**), and $|\chi^{(3)}_{\pm\Omega_2, \pm\Omega_2}(\omega)|^2$ (**d**) based upon the three-level model, which correspond to the intensity spectra for oscillations A, B, and C, respectively. The error bars indicate the standard deviation of the least-squares fit. **e** The optical process corresponding to $\chi^{(3)}_{\pm\Omega_1, \pm\Omega_1}(\omega)$ (oscillation A). The probe pulse produces a transition from the ground state $|GS\rangle$ to the ∓ 1-phonon-dressed state, $|IM_f, \mp 1\rangle$, and the light emission associated with a transition from $|IM_f, \pm 1\rangle$ to $|GS\rangle$ occurs. It generates the oscillatory component whose frequency equals twice the frequency of the phonon.

Using Eq. (6) and the photon-energy dependence of $|\Delta I_{\Omega_a+\Omega_b}(\omega)|^2$ experimentally obtained, we deduce the $|\chi^{(3)}_{\pm\Omega_a,\pm\Omega_b}(\omega)|^2$ spectra of oscillations A–C, which are shown by red and blue circles in Fig. 5b–d. The three spectra all show two peaks around 1.8 and 2.1 eV, although the data points vary to some extent. The energy difference between the two peaks, ~0.3 eV, is almost equal to double the intramolecular vibration frequency ($2\hbar\Omega_1 = 0.29$ eV and $2\hbar\Omega_2 = 0.33$ eV). In addition, the energy gravity of the two peaks, 1.95 eV, is close to the intramolecular transition energy (Fig. 2a). These are consistent with the situation shown in Figs. 1a and 4. Thus, the two obtained peaks are attributed to ±1-phonon-dressed states of the one-photon-forbidden intramolecular excited state $|IM_f\rangle$, and $|IM_f\rangle$ is located at almost the same energy with the one-photon allowed state $|IM_a\rangle$ as expected.

Simulations of probe photon-energy dependence of oscillatory signals. To confirm the interpretations proposed in the preceding section, we formulated the nonlinear optical susceptibility $\chi^{(3)}_{\pm\Omega_a,\pm\Omega_b}(\omega)$ by using the perturbation treatment in the framework of the third-order nonlinear optics. In this formulation, we adopted the three-level model mentioned above, which includes the intramolecular excited states $|IM_a\rangle$ and $|IM_f\rangle$, and the ground state $|GS\rangle$ in each dimer and considered that the phonon-dressed states of these excited states are formed by periodic perturbation to electrons via the EMV coupling. The specific expression of $\chi^{(3)}_{\pm\Omega_a,\pm\Omega_b}(\omega)$ is shown in the Methods section.

Using the experimentally obtained energy ($\hbar\omega_{IMa} = 1.99$eV) and damping constant ($\hbar\gamma_{IMa} = 0.111$ eV) of $|IM_a\rangle$ (Fig. 2a), and assuming the energy ($\hbar\omega_{IMf} = 1.97$eV) and damping constant ($\hbar\gamma_{IMf} = 0.08$ eV) of $|IM_f\rangle$, we simulate the $|\chi^{(3)}_{\pm\Omega_a,\pm\Omega_b}(\omega)|^2$ spectra for the three kinds of oscillations A–C, which are shown by the solid red and blue lines in Fig. 5b–d. The procedures of the simulations are detailed in Supplementary Note 5. The energy differences between two peaks for $|\chi^{(3)}_{\pm\Omega_1,\pm\Omega_1}(\omega)|^2$ (Fig. 5b), for $|\chi^{(3)}_{\pm\Omega_1,\pm\Omega_2}(\omega)|^2$ (Fig. 5c), and for $|\chi^{(3)}_{\pm\Omega_2,\pm\Omega_2}(\omega)|^2$ (Fig. 5d) are equal to $2\hbar\Omega_1$, $\hbar(\Omega_1+\Omega_2)$, and $2\hbar\Omega_2$, respectively, which are shown by the double-headed arrows in each panel. These $|\chi^{(3)}_{\pm\Omega_a,\pm\Omega_b}(\omega)|^2$ spectra almost reproduce the experimental intensity spectra of oscillations A-C. This demonstrates that ±1-phonon-dressed states are responsible for the observed oscillatory signals.

Discussions

Here, we discuss the nature of observed phonon-dressed states based on the Floquet theory. According to the theory, the periodic potential of an infrared-active phonon creates new one-photon allowed states, $|IM_a, \pm 2n\rangle$ and $|IM_f, \pm(2n-1)\rangle$ (n: natural number), around the original states, $|IM_a\rangle$ and $|IM_f\rangle$, respectively. In our case, $2\Omega_1$ and $2\Omega_2$, which are twice the intramolecular vibration frequencies, are comparable to a half of the spectral width of the probe pulse, ~0.25 eV, and thus we can observe only $|IM_f, \pm 1\rangle$ through light emission. The two optical processes shown in Fig. 5e are the origins of $\chi^{(3)}_{\Omega_1,\Omega_1}(\omega)$ and $\chi^{(3)}_{-\Omega_1,-\Omega_1}(\omega)$, which generates the peaks of oscillation A located at $\hbar\omega_{IMf}+\hbar\Omega_1$ and $\hbar\omega_{IMf}-\hbar\Omega_1$, respectively. This is the reason why all high-frequency components, associated with phonon-dressed states, have peaks situated at energy of $|IM_f, \pm 1\rangle$. More strictly, the peaks of oscillation B should appear at $\hbar\omega_{IMf}\pm\hbar\Omega_1$

and $\hbar\omega_{IMf}\pm\hbar\Omega_2$, whereas only two peaks are observed in Fig. 5c. This is because the intramolecular excited state has a broad spectral width (~0.2 eV) (Fig. 2a). The detailed formulation of phonon-dressed states based on the Floquet theory is reported in Supplementary Notes 6 and 7.

In summary, we investigated the phonon-dressed states in a half-filled organic Mott insulator. Under molecular dimerization, the a_g modes of intramolecular vibrations became infrared-active and modulated the energy levels of π-molecular orbitals via EMV couplings. Using this feature, we added strong periodic potentials to the π-molecular orbitals by exciting a couple of a_g modes. Through sub-cycle spectroscopy with a mid-infrared pump pulse and an ultrashort visible-probe pulse, we observed optical radiation with the second-order oscillatory components of two a_g modes. From the analyses of their probe-energy dependences, we demonstrated that phonon-dressed states of the one-photon-forbidden intramolecular excited state were formed and responsible for the characteristic optical radiation. Our method of combining coherent phonon excitations and ultrafast sub-cycle spectroscopy can be used for advanced studies of Floquet states and further phase controls in various types of molecular materials.

Methods

Sample preparations. Single crystals of K-TCNQ were grown from KI and TCNQ through slow diffusion in acetonitrile according to the literature[31]. The typical crystal size was approximately 5 mm × 0.5 mm × 0.5 mm. Almost the same data are obtained in distinct samples.

Steady-state optical spectroscopy measurements. The polarized reflectivity (R) spectrum in a single crystal of K-TCNQ was measured using a specially designed spectrometer with a 25-cm-grating monochromator in the visible and near-infrared region (0.5–5.0 eV) and a Fourier-transform infrared spectrometer in the mid-infrared region (0.08–1.2 eV). Both of these spectrometers were equipped with an optical microscope. The spectra of the real (ε_1) and imaginary (ε_2) parts of the complex dielectric constant were obtained from the polarized R spectra using the Kramers–Kronig transformation.

Mid-infrared-pump visible-probe reflectivity measurements. To perform the mid-infrared-pump visible-probe reflectivity measurements, we employed a Ti:sapphire regenerative amplifier (RA) with a central photon energy of 1.55 eV, a repetition rate of 1 kHz, a pulse duration of 35 fs, and a pulse energy of 7.5 mJ as the light source. The output of the RA is divided into two beams, which were used to generate ultrashort visible pulses and carrier-envelope-phase (CEP)-stable mid-infrared pulses.

To generate an ultrashort probe pulse, we used a hand-made non-collinear optical parametric amplifier (NOPA)[32], which was excited by one beam from the RA (pulse energy 3.5 mJ). In the NOPA, we further divided the output of RA into two beams. One was focused on a sapphire crystal, from which broadband white light was generated. The other was converted to second-harmonic light in a second-order nonlinear crystal, β-BaB₂O₄. Another β-BaB₂O₄ crystal was used to enhance the white light via non-collinear optical parametric amplification, in which the second-harmonic light and white light were used as pump light and seed light, respectively. The pulse width was approximately 8 fs and the spectrum range was from 1.75 to 2.25 eV. The temporal profile of the pulse was measured by second-harmonic-generation frequency-resolved-optical-gating using the retrieval algorithm[33,34]. The fundamental and second-harmonic spectra of the pulse were measured by a spectroscope, the sensitivity of which was calibrated using a well-calibrated deuterium-halogen lamp.

A CEP-stable mid-infrared pulse was obtained by difference-frequency generation (DFG) between the idler outputs of two optical parametric amplifiers (OPA1 and OPA2) excited by another output of the RA (pulse energy 4.0 mJ). OPA1 delivered 1640 nm pulses with 390 μJ energy, and OPA2 delivered pulses tuneable from 1900 to 2080 nm with 120 μJ energy. We obtained mid-infrared pulses with Type I DFG in a GaSe crystal of thickness 500 μm between two pulses generated from OPA1 and OPA2. The GaSe crystal was placed at an external phase-matching angle of approximately 34°[35,36]. By tuning the wavelength of the output from OPA2, we obtained two types of mid-infrared pulses for pumps I and II, as shown in Fig. 2b. To stabilize the long-term CEP of the mid-infrared pulses, we performed feedback controls of the optical path lengths by using a pair of CaF₂ wedge plates inserted after OPA2 and adjusting two delay lines[37]. The CEP stability of the controlled mid-infrared pulses was within ±1 fs over a few tens of hours at the sample position.

The electric-field waveform of the mid-infrared pulse was measured using an electro-optic sampling (EOS) method. For this measurement, a 20-μm-thick LiGaS$_2$ (LGS) crystal was used as a second-order nonlinear crystal, and the output of NOPA was used as a sampling pulse. The detection wavelength range of EOS was limited due to the absorptions of LGS and water vapor; electric fields of pulses with wavelengths longer than 12 μm or of 5.5–7.7 μm cannot be detected. The maximum electric-field amplitude of the mid-infrared pulse, E_{MIR}, was evaluated from a spatial intensity profile obtained by a knife-edge method, and an electric-field profile obtained from EOS and the fluence of the pulse. The maximum electric field E_{MIR} (fluence) of the pulses for pumps I and II were 8.07 MV cm^{-1} (500 nJ) and 8.79 MV cm^{-1} (1000 nJ), respectively. The amplitude of the mid-infrared pulse was weakened by a pair of wire-grid polarizers.

For the mid-infrared-pump visible-probe reflectivity measurements, the polarization of the electric field E_{MIR} (E_{VIS}) of the mid-infrared pump pulse (visible-probe pulse) was set parallel (perpendicular) to the a-axis. The intensity of the reflection light, including the emission from the phonon-dressed states, was detected by a silicon photodiode. We inserted a bandpass filter with a full width at half maximum of approximately 40 meV in front of the detector to select the probe photon energy $\hbar\omega$. The delay time of the probe pulse relative to the mid-infrared pulse was controlled by a delay stage.

Fitting analyses of high-frequency components of reflectivity changes. To obtain detailed information about the oscillatory signals, we perform a fitting analysis of the oscillatory components, $\Delta I_{HF}(t_d)/I_R$ and $\Delta I_{LF}(t_d)/I_R$, with the following formula:

$$\frac{\Delta I_{HF}(t_d)}{I_R} = \mathrm{HPF}\left\{ \sum_{\lambda=1}^{2} \alpha_{\lambda\lambda}\left[e_{MIR}(t_d) \otimes f_\lambda(t_d)\right]^2 \right.$$
$$\left. + 2\alpha_{12}\left[e_{MIR}(t_d) \otimes f_1(t_d)\right]\left[e_{MIR}(t_d) \otimes f_2(t_d)\right] \right\} \tag{7}$$

$$\frac{\Delta I_{LF}(t_d)}{I_R} = \mathrm{LPF}\left\{ 2\beta_{12}\left[e_{MIR}(t_d) \otimes f_1(t_d)\right]\left[e_{MIR}(t_d) \otimes f_2(t_d)\right]\right\} \tag{8}$$
$$f_\lambda(t_d) = \exp\left(-\frac{t_d}{T_\lambda}\right)\sin(\Omega_\lambda t_d + \phi_\lambda)\theta(t_d)$$

Here, $e_{MIR}(t_d)$ is a normalized electric-field waveform of a mid-infrared pulse. $f_\lambda(t_d)$ expresses a damped oscillator λ with frequency Ω_λ. ϕ_λ and T_λ are the initial phase and relaxation time of oscillator λ, respectively. $\theta(t_d)$ is a unit step function. HPF (LPF) is an operator that extracts a high- (low-)frequency component from the $\Delta I_R(t_d)/I_R$ signals. $\otimes$ shows a convolution integral. $e_{MIR}(t_d) \otimes f_\lambda(t_d)$ expresses the dynamics of a normal mode of the oscillator λ, $Q_\lambda(t_d)$. α_{11}, α_{12}, α_{22}, and β_{12} show the amplitudes of oscillations A, B, C, and D, with frequencies of Ω_A, Ω_B, Ω_C, and Ω_D, respectively. Using Eqs. (7) and (8), the experimental high-frequency oscillation (red line) is well reproduced (black line in Fig. 2j). Furthermore, power spectra (red circles) of the low- and high-frequency oscillations in Fig. 3a, b are also reproduced as shown by the black solid lines, which validates the fitting using Eqs. (7) and (8). This fitting can clearly separate the high-frequency components into oscillations A–C (colored lines in Fig. 3c). Full analyses, including the low-frequency and background components of $\Delta I_R(t_d)/I_R$, are reported in Supplementary Note 2.

Expression of third-order nonlinear susceptibility. In the three-level model in which the intramolecular excited states $|IM_a\rangle$ and $|IM_f\rangle$, and the ground state $|GS\rangle$ are taken into account, $\chi^{(3)}_{\pm\Omega_a, \pm\Omega_b}(\omega)$ is obtained from the perturbation theory as follows:

$$\chi^{(3)}_{\pm\Omega_a, \pm\Omega_b}(\omega) \equiv \chi^{(3)}\left(\pm\Omega_a, \pm\Omega_b, \omega \mp \Omega_a \mp \Omega_b\right) \tag{9a}$$

$$\chi^{(3)}(\omega_1, \omega_2, \omega_3)$$
$$\propto \left[\frac{1}{(\omega_{IMa} - \omega_1 - \omega_2 - \omega_3 - i\gamma_{IMa})(\omega_{IMf} - \omega_2 - \omega_3 - i\gamma_{IMf})(\omega_{IMa} - \omega_3 - i\gamma_{IMa})} \right.$$
$$\left. + \frac{1}{(\omega_{IMa} - \omega_1 - \omega_2 - \omega_3 - i\gamma_{IMa})(\omega_{IMf} - \omega_1 - \omega_3 - i\gamma_{IMf})(\omega_{IMa} - \omega_3 - i\gamma_{IMa})} \right] \tag{9b}$$

Here, $\hbar\omega_{IMa}$ ($\hbar\omega_{IMf}$) and $\hbar\gamma_{IMa}$ ($\hbar\gamma_{IMf}$) are the energy and the damping constant of the state $|IM_a\rangle$ ($|IM_f\rangle$), respectively. The details of the derivations are reported in Supplementary Note 4.

Data availability
The data that support the findings of this study are available from the corresponding author upon reasonable request.

Code availability
The codes are available from the corresponding author upon reasonable request.

References
1. Shirley, J. H. Solution of the Schrödinger equation with a Hamiltonian periodic in time. *Phys. Rev.* **138**, B979–B987 (1965).
2. Oka, T. & Kitamura, S. Floquet engineering of quantum materials. *Annu. Rev. Condens. Matter Phys.* **10**, 387–408 (2019).
3. Giovannini, U. D. & Hübener, H. Floquet analysis of excitations in materials. *J. Phys. Mater.* **3**, 012001 (2020).
4. Mysyrowicz, A. et al. "Dressed excitons" in a multiple-quantum-well structure: evidence for an optical stark effect with femtosecond response time. *Phys. Rev. Lett.* **56**, 2748–2751 (1986).
5. Johnsen, K. & Jauho, A. P. Quasienergy spectroscopy of excitons. *Phys. Rev. Lett.* **83**, 1207–1210 (1999).
6. Wang, Y. H., Steinberg, H., Jarillo-Herrero, P. & Gedik, N. Observation of Floquet-Bloch states on the surface of a topological insulator. *Science* **342**, 453–457 (2013).
7. Sie, E. J. et al. Valley-selective optical Stark effect in monolayer WS$_2$. *Nat. Mater.* **14**, 290–294 (2015).
8. Uchida, K. et al. Subcycle optical response caused by a terahertz dressed state with phase-locked wave functions. *Phys. Rev. Lett.* **117**, 277402 (2016).
9. McIver, J. W. et al. Light-induced anomalous Hall effect in graphene. *Nat. Phys.* **16**, 38–41 (2020).
10. Nagai, K. et al. Dynamical symmetry of strongly light-driven electronic system in crystalline solids. *Commun. Phys.* **3**, 137 (2020).
11. Autler, S. H. & Townes, C. H. Stark effect in rapidly varying fields. *Phys. Rev.* **100**, 703–722 (1955).
12. Fluegel, B. et al. Femtosecond studies of coherent transients in semiconductors. *Phys. Rev. Lett.* **59**, 2588–2591 (1987).
13. Knox, W. H., Chemla, D. S., Miller, D. A. B., Stark, J. B. & Schmitt-Rink, S. Femtosecond ac Stark effect in semiconductor quantum wells: extreme low- and high-intensity limits. *Phys. Rev. Lett.* **62**, 1189–1192 (1989).
14. Maeda, A. et al. Large optical nonlinearity of semiconducting single-walled carbon nanotubes under resonant excitations. *Phys. Rev. Lett.* **94**, 047404 (2005).
15. Kono, J. et al. Resonant terahertz optical sideband generation from confined magnetoexcitons. *Phys. Rev. Lett.* **79**, 1758–1761 (1997).
16. Wagner, M. et al. Resonant enhancement of second order sideband generation for intraexcitonic transitions in GaAs/AlGaAs multiple quantum wells. *Appl. Phys. Lett.* **94**, 241105 (2009).
17. Zaks, B., Liu, R. B. & Sherwin, M. S. Experimental observation of electron-hole recollisions. *Nature* **483**, 580–583 (2012).
18. Zaks, B., Banks, H. & Sherwin, M. S. High-order sideband generation in bulk GaAs. *Appl. Phys. Lett.* **102**, 012104 (2013).
19. Langer, F. et al. Lightwave-driven quasiparticle collisions on a subcycle timescale. *Nature* **533**, 225–229 (2016).
20. Banks, H. B. et al. Dynamical birefringence: electron-hole recollisions as probes of Berry curvature. *Phys. Rev. X.* **7**, 041042 (2017).
21. Langer, F. et al. Lightwave valleytronics in a monolayer of tungsten diselenide. *Nature* **557**, 76–80 (2018).
22. Hübener, H., Giovannini, D. G. & Rubio, A. Phonon driven floquet matter. *Nano Lett.* **18**, 1535–1542 (2018).
23. Shin, D. et al. Phonon-driven spin-Floquet magneto-valleytronics in MoS$_2$. *Nat. commun.* **9**, 638 (2018).
24. Konno, M., Ishii, T. & Saito, Y. The crystal structures of the low and high-temperature modifications of potassium 7,7,8,8-tetraeyanoquinodimethanide. *Acta Cryst. B* **33**, 763–770 (1977).
25. Lépine, Y., Caillé, A. & Larochelle, V. Potassium-tetracyanoquinodimethane (K-TCNQ): a spin-Peierls system. *Phys. Rev. B* **18**, 3585–3592 (1978).
26. Painelli, A. & Girlando, A. Electron-molecular vibration (e-mv) coupling in charge-transfer compounds and its consequences on the optical spectra: a theoretical framework. *J. Chem. Phys.* **84**, 5655–5671 (1986).
27. Yakushi, K., Kusaka, T. & Kuroda, H. Low-temperature reflection spectrum of K-TCNQ single crystal. *Chem. Phys. Lett.* **68**, 139–142 (1979).
28. Khvostenko, O. G., Kinzyabulatov, R. R., Khatymova, L. Z. & Tseplin, E. E. The lowest triplet of tetracyanoquinodimethane via UV−vis absorption spectroscopy with Br-containing solvents. *J. Phys. Chem. A* **121**, 7349–7355 (2017).
29. Tanner, D. B., Jacobsen, C. S., Bright, A. A. & Heeger, A. J. Infrared studies of the energy gap and electron-phonon interaction in potassium-tetracyanoquinodimethane (K-TCNQ). *Phys. Rev. B* **16**, 3283–3290 (1977).
30. Painelli, A., Girlando, A. & Pecile, C. Accurate electron-molecular vibration coupling constants from powders optical spectra: TCNQ and TTF. *Solid State Commun.* **52**, 801–806 (1984).

31. Singh, Y., Goswami, D. P., Bala, M. & Kalra, M. L. Large needle-shaped highly conducting organic charge transfer complexes with asymmetric donor molecules. *J. Cryst. Growth* **123**, 601–604 (1992).

32. Adachi, S., Watanabe, Y., Sudo, Y. & Suzuki, T. Few-cycle pulse generation from noncollinear optical parametric amplifier with static dispersion compensation. *Chem. Phys. Lett.* **683**, 7–11 (2017).

33. DeLong, K. W., Trebino, R., Hunter, J. & White, W. E. Frequency-resolved optical gating with the use of second-harmonic generation. *J. Opt. Soc. Am. B* **11**, 2206–2215 (1994).

34. Trebino, R. et al. Measuring ultrashort laser pulses in the time-frequency domain using frequency-resolved optical gating. *Rev. Sci. Instrum.* **68**, 3277–3295 (1997).

35. Sell, A., Leitenstorfer, A. & Huber, R. Phase-locked generation and field-resolved detection of widely tunable terahertz pulses with amplitudes exceeding 100 MV/cm. *Opt. Lett.* **33**, 2767–2769 (2008).

36. Bai, Y. et al. Intense broadband mid-infrared pulses of 280 MV/cm for supercontinuum generation in gaseous medium. *Opt. Lett.* **43**, 667–670 (2018).

37. Yamakawa, T. et al. Long-term stabilization of carrier envelope phases of mid-infrared pulses for the precise detection of phase-sensitive responses to electromagnetic waves. *AIP Adv.* **10**, 025311 (2020).

Acknowledgements

Author contributions

N.S., T.K., T.Y., D.S., T. Morimoto, and T. Miyamoto built the mid-infrared-pump visible-probe spectroscopy system. N.S., T.K., T.Y., D.S., and T. Miyamoto carried out the pump-probe experiments of K-TCNQ. H.O. prepared the sample. N.S. and T.K. analyzed the experimental data. T.O. formulated and performed the simulation of the data. H.O. coordinated the study. The manuscript was written by N.S., T.O., T. Miyamoto, and H.O. with inputs from all authors.

Competing interests

The authors declare no competing interests.

Additional information

Supplementary information The online version contains supplementary material available at https://doi.org/10.1038/s42005-022-00838-x.

Correspondence and requests for materials should be addressed to Tatsuya Miyamoto or Hiroshi Okamoto.

Peer review information *Communications Physics* thanks the anonymous reviewers for their contribution to the peer review of this work. Peer reviewer reports are available.

Reprints and permission information is available at http://www.nature.com/reprints

Publisher's note Springer Nature remains neutral with regard to jurisdictional claims in published maps and institutional affiliations.